Statistical Characterization and Computationally Efficient Modeling of a Class of Underwater Acoustic Communication Channels

Parastoo Qarabaqi, *Student Member, IEEE*, and Milica Stojanovic, *Fellow, IEEE*

Abstract—Underwater acoustic channel models provide a tool for predicting the performance of communication systems before deployment, and are thus essential for system design. In this paper, we offer a statistical channel model which incorporates physical laws of acoustic propagation (frequency-dependent attenuation, bottom/surface reflections), as well as the effects of inevitable random local displacements. Specifically, we focus on random displacements on two scales: those that involve distances on the order of a few wavelengths, to which we refer as small-scale effects, and those that involve many wavelengths, to which we refer as large-scale effects. Small-scale effects include scattering and motion-induced Doppler shifting, and are responsible for fast variations of the instantaneous channel response, while large-scale effects describe the location uncertainty and changing environmental conditions, and affect the locally averaged received power. We model each propagation path by a large-scale gain and micromultipath components that cumulatively result in a complex Gaussian distortion. Time- and frequency-correlation properties of the path coefficients are assessed analytically, leading to a computationally efficient model for numerical channel simulation. Random motion of the surface and transmitter/receiver displacements introduce additional variation whose temporal correlation is described by Bessel-type functions. The total energy, or the gain contained in the channel, averaged over small scale, is modeled as log-normally distributed. The models are validated using real data obtained from four experiments. Specifically, experimental data are used to assess the distribution and the autocorrelation functions of the large-scale transmission loss and the short-term path gains. While the former indicates a log-normal distribution with an exponentially decaying autocorrelation, the latter indicates a conditional Ricean distribution with Bessel-type autocorrelation.

Index Terms—Channel simulation, Doppler shifting, Doppler spreading, frequency correlation, large-scale fading, scattering, small-scale fading, statistical channel modeling, time correlation, underwater acoustic (UWA) communications.

I. INTRODUCTION

UNDERWATER ACOUSTIC (UWA) communication systems have to be designed to operate in a variety of conditions that differ from the nominal ones due to the

The authors are with the Department of Electrical and Computer Engineering, Northeastern University, Boston, MA 02115 USA (e-mail: qarabaqi@ece.neu.edu; millitsa@ece.neu.edu).

changes in system geometry and environmental conditions. To allocate the appropriate resources (power, bandwidth) before system deployment, as well as to design appropriate signals and processing algorithms on both the physical link layer and the higher network layers, it is necessary to have a relatively accurate channel model. Beam tracing tools, such as Bellhop [1], use ray theory to provide an accurate deterministic picture of a UWA channel for a given geometry and signal frequency, but they do not take into account random channel variation. In recent years, there has been a growing awareness of the need to develop statistical channel models that will lead to computationally efficient tools for numerical simulation. New tools have been developed that address this need to some extent. For example, the Virtual Timeseries EXperiment (VirTEX) code [2] was developed to simulate the effect of channel variation in a manner that is computationally more efficient than repeated application of the Bellhop beam tracing. This algorithm operates by tracing multiple interrelated beams to assess the cumulative effect on the signal of a given frequency. However, its computational complexity may still be an issue. For example, simulating a channel with a Doppler distortion on the order of 15 Hz requires at least 30 channel realizations per second which amounts to a total of 5400 Bellhop runs for simulating a system with two transmitters and six receiver elements over a period of 15 s. The wave front model [3] offers a deterministic approach which provides approximations to the ray theory to efficiently model the effects of the curvature of the surface waves and the amplitude and arrival time fluctuations that they introduce [4].

Numerous studies have also been conducted to model the UWA channel stochastically, e.g., [5]–[16]. These studies are usually based on the analyses of experimental acoustic data collected in a particular location. Some authors find Ricean fading [5], [7] or Rayleigh fading [6], [8], [13] to provide a good match for their measurements, while others find log-normal distribution [9], [10], the K-distribution [11], [12], or a general class of Ricean shadowed distribution [16] to be a better fit. The variety of proposed statistical models is due to experiment-specific properties, e.g., the deployment site and the type of signals used for probing, as well as the time intervals during which the channel is observed.

Statistical modeling of small-scale phenomena is a subject of ongoing research, which points to different types of fading, and no consensus exists yet on this topic. Modeling of large-scale phenomena has also been addressed only to a very limited extent (see, e.g., [14], which shows some evidence of log-normal fading), while a few attempts have been made at unifying the

small- and large-scale models (see, e.g., [5], [11], and [15]). In [14], knowledge of the environmental conditions at an experiment site was used to repeatedly run the Bellhop model to generate an ensemble of channel responses which was then used to estimate the statistical properties of the channel. The changing environmental conditions which were taken into account included water temperature and salinity. The results obtained through the Bellhop channel simulator showed statistical properties similar to those obtained experimentally; however, an accurate agreement was not observed. This mismatch may be because only partial knowledge of the environmental conditions was used, and surface variation was not taken into account. In [17], Heitsenrether and Badiey used the environmental data obtained from an acoustic experiment to generate varying surface shapes, which were then imported into the Bellhop beam tracer to generate the corresponding acoustic field. The simulated data were compared to the experimental measurements and a good agreement was observed for calm ocean conditions. At high wind speeds, however, the simulation results deviated from the experimental measurements. This deviation may be caused by the inability of the surface shape generator to model breaking waves which occur at high wind speeds, causing formation of bubble clouds, as well as acoustic focusing by wave curvature [18]. Formation of bubbles near the water surface was found in [19] to be the underlying cause for the changing behavior of the UWA channels at different wind speeds. The radius and the density of bubbles that are generated at different wind conditions, as well as their acoustical properties, were studied. Such knowledge can be used to further improve the existing UWA channel models.

The goal of our study is to provide a mathematically rigorous analytical model that takes into account certain physical aspects of acoustic propagation, and to validate such a model using experimental data. In parallel, our goal is also to develop a numerically efficient simulation model that describes the channel response in a wide range of frequencies representative of an acoustic communication system. Toward this goal, we distinguish two types of channel variations: those that are caused by displacements spanning many wavelengths, and those that are caused by displacements on the order of one or a few wavelengths. We refer to the former as large-scale variations, and to the latter as small-scale variations. Large-scale variations are modeled as a consequence of system displacements that cannot be predicted using the nominal system geometry. Namely, while a nominal transmitter and receiver placement within a fixed system geometry and a fixed sound-speed profile will yield a fixed acoustic field, the actual field will vary due to *uncertainty* about the exact system geometry. Such an uncertainty is treated as random, leading to large-scale variation in the gains and delays of propagation paths. At the same time, once a particular large-scale displacement is *given*, additional small-scale variation will occur in the path gains and delays. This variation is modeled as a consequence of scattering and instantaneous motion. Considering motion on the order of 1 m/s, and frequencies on the order of 10 kHz, a wavelength is traversed during a subsecond interval. Such short intervals of time incidentally correspond to typical communication transactions (a packet or a frame of packets). Small-scale channel variations

can thus be thought of as those variations that occur over a communication transaction. They are to be distinguished from the variations that are caused by larger system displacements that span many wavelengths and occur on correspondingly longer intervals of time. Small-scale variations influence the instantaneous channel response, and, consequently, the instantaneous signal-to-noise ratio (SNR). As such, they are meaningful for the analysis of signal processing algorithms and network protocols, and the assessment of average bit error rate or packet error rate, conditioned on a particular large-scale realization. In contrast, large-scale variations influence the SNR through its local average, causing it to vary over longer periods of time. As such, they are meaningful for the analysis of top-level system functions such as power allocation and the assessment of outage probabilities and statistical coverage.

The rest of this paper is organized as follows. In Section II, we overview the basics of acoustic propagation that lead to the notion of a nominal channel response, and we introduce a model for the large-scale channel variation. Small-scale channel effects are modeled in Section III, while motion-induced Doppler effects are addressed in Section IV. Section V discusses the impact of these random effects on the overall channel gain. Experimental results are presented in Section VI, and conclusions are summarized in Section VII.

II. NOMINAL CONDITIONS AND LARGE-SCALE UNCERTAINTY

A. Nominal Conditions: Decoupling Path Filtering From Path Gains

Nominal channel geometry, along with a specified sound-speed profile, gives rise to the nominal response of an acoustic channel. This response characterizes a time-invariant system, and it can be assessed by beam tracing for typical acoustic communication frequencies.

The basic path loss experienced by a signal of frequency f traveling over distance l affects the received signal energy and is given by [20]

$$A(l, f) = A_0 l^k \mathrm{a}(f)^l \tag{1}$$

where A_0 is a scaling constant, k is the spreading factor, and $\mathrm{a}(f)$ is the absorption coefficient, which can be obtained in decibels per kilometer using the Thorp's empirical formula [20, Ch. 1] as

$$0.11 \frac{f^2}{1 + f^2} + 44 \frac{f^2}{4100 + f^2} + 2.75 \times 10^{-4} f^2 + 0.003$$

where f is in kilohertz. Considering multiple propagation paths of nominal length $\bar{l}_p$, $p = 0, \dots, P - 1$, each path will act as a lowpass filter, whose transfer function, which affects the amplitude of the received signal, can be modeled as

$$\bar{H}_p(f) = \frac{\Gamma_p}{\sqrt{A(\bar{l}_p, f)}} \tag{2}$$

where Γ_p is the cumulative reflection coefficient encountered over n_{sp} surface and n_{bp} bottom reflections along the pth path.

For example, an ideal surface can be modeled by a reflection coefficient $\gamma_s = -1$, while each bottom reflection can be modeled by [20, Ch. 3]

$$\gamma_b(\theta_p) = \begin{cases} \dfrac{\rho_b \sin\theta_p - \rho\sqrt{\left(\dfrac{c}{c_b}\right)^2 - \cos^2\theta_p}}{\rho_b \sin\theta_p + \rho\sqrt{\left(\dfrac{c}{c_b}\right)^2 - \cos^2\theta_p}}, & \cos\theta_p \le \dfrac{c}{c_b} \\[4mm] 1, & \text{otherwise} \end{cases}$$
(3)

where θ_p is the grazing angle associated with the pth propagation path, ρ and c are the density and the speed of sound in water ($\rho = 1000$ kg/m^3 and $c = 1500$ m/s, nominally), and ρ_b and c_b are the density and the speed of sound in bottom. For soft bottom, $c_b < c$, so that critical reflection never occurs.

Given the transfer function of each path, the overall transfer function of the multipath channel is obtained as

$$\bar{H}(f) = \sum_p \bar{H}_p(f) e^{-j2\pi f \bar{\tau}_p}$$
(4)

where $\bar{\tau}_p$ is the propagation delay associated with the pth path, i.e., $\bar{\tau}_p = \bar{l}_p/c - t_0$ for constant sound speed, measured in reference to some t_0, e.g., $t_0 = \bar{l}_0/c$.

In general, each path is characterized by an impulse response of a *different* shape, and this fact prevents one from obtaining a tractable, simple channel model. To explore simplified versions, we examine an approximation to the function $\bar{H}_p(f)$. In particular, let us express this function so as to include the dependence on the reference path $p = 0$

$$\bar{H}_p(f) = \frac{\Gamma_p}{\sqrt{\left(\dfrac{\bar{l}_p}{\bar{l}_0}\right)^k \mathsf{a}(f)^{\bar{l}_p - \bar{l}_0}}} \bar{H}_0(f).$$
(5)

Fig. 1 shows the reference function $\bar{H}_0(f)$ for $\bar{l}_0 = 1$ km and $k = 2$.

The frequency-dependence that distinguishes the pth path from the reference path is embodied in the term $\mathsf{a}(f)^{\bar{l}_p - \bar{l}_0}$ in (5). If this term could be approximated as constant, one could model all the paths by an impulse response of the *same* shape, and just a different gain. The fact that the absorption factor $\mathsf{a}(f)$ has a value very close to 1 for a broad range of acoustic communication frequencies may justify an approximation of the form

$$\mathsf{a}(f)^{-(\bar{l}_p - \bar{l}_0)/2} \approx \mathsf{a}_0^{-(\bar{l}_p - \bar{l}_0)/2}$$
(6)

where a_0 is the absorption factor corresponding to a frequency within the signal bandwidth $[f_0, f_0 + B]$. We examine the viability of such an approximation in Fig. 2. This figure shows the factor $\mathsf{a}(f)^{-\Delta\bar{l}_p/2}$ as a function of frequency, for several path length differences $\Delta\bar{l}_p = \bar{l}_p - \bar{l}_0$. While the dependence on $\Delta\bar{l}_p$ is exponential, the spacing between the curves appears to be linear because $\mathsf{a}(f)$ is very close to 1, i.e.,

$$\mathsf{a}(f)^{-\Delta\bar{l}_p/2} = [1 + \epsilon(f)]^{-\Delta\bar{l}_p/2} \approx 1 - \epsilon(f)\Delta\bar{l}_p/2.$$

The values shown range only between about 0.9 and 1, indicating that the approximation (6) may indeed be valid, espe-
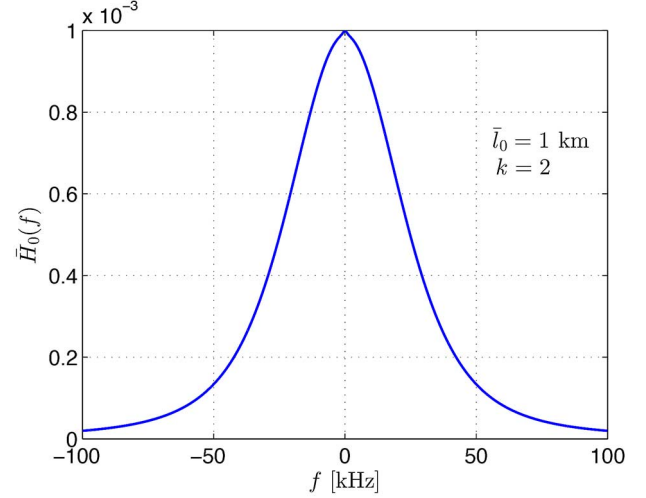

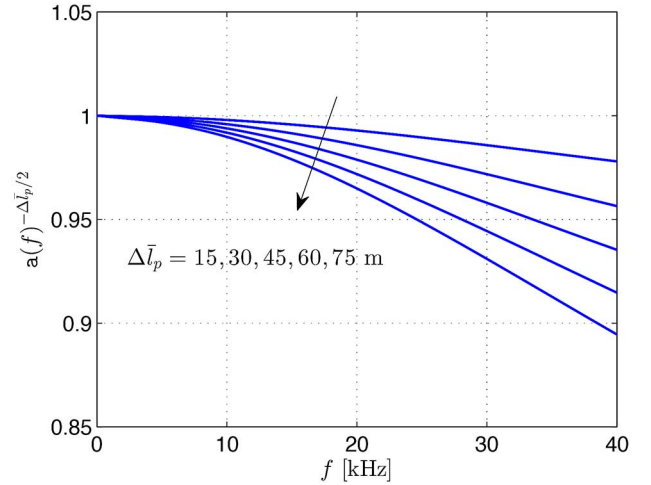Fig. 1. Reference path transfer function $\bar{H}_0(f)$.

Fig. 2. Verifying the approximation (6). Note that one needs to focus only on the frequency range occupied by a given system. For example, if a system operates in the 10–20-kHz acoustic band, the factor $\mathsf{a}(f)^{-\Delta\bar{l}_p/2}$ varies only between 1 and 0.98 for $\Delta\bar{l}_p$ up to 40 m.

cially for small path length differences. The smallest path length difference shown, 15 m, corresponds to the relative path delay of 10 ms, a value that is within the multipath spread of the majority of shallow-water channels. Note also that it suffices to judge the validity of our approximation only within the frequency range occupied by a given system. For example, if a system operates in the 10–20-kHz acoustic band, the factor $\mathsf{a}(f)^{-\Delta\bar{l}_p/2}$ varies only between 1 and 0.98 for $\Delta\bar{l}_p$ up to 40 m.

Using the approximation (6), we model the channel transfer function as

$$\bar{H}_p(f) \approx \bar{h}_p \bar{H}_0(f)$$
(7)

where the path gain is given by

$$\bar{h}_p = \frac{\Gamma_p}{\sqrt{\left(\dfrac{\bar{l}_p}{\bar{l}_0}\right)^k \mathsf{a}_0^{\bar{l}_p - \bar{l}_0}}}.$$
(8)

The constant a_0 may be taken as the absorption factor at any frequency within the operational bandwidth, e.g., the center frequency f_c, or the lower/upper band-edge frequency, resulting

in maximal/minimal path gain, respectively. Any choice should be fine, since the assumption is that $\mathsf{a}(f)$ does not change much over a typical bandwidth of an acoustic communication system.

From our discussion so far, it seems reasonable to adopt a channel model in which the effects of path filtering and multipath are *decoupled* such that each path contributes with a gain $\bar{h}_p$ and delay $\bar{\tau}_p$, while the filtering effect is the same for all the paths, and described by the function $\bar{H}_0(f)$. The overall channel transfer function is thus given by

$$\bar{H}(f) = \bar{H}_0(f) \sum_p \bar{h}_p e^{-j2\pi f \bar{\tau}_p}. \tag{9}$$

B. Large-Scale Displacements (Location Uncertainty)

Transmitter/receiver displacements within a nominal channel geometry, as well as changes in the surface height (e.g., due to tides) or shape of the bottom, lead to an uncertainty about the exact system geometry. These displacements effectively cause the path length to deviate from the nominal as $l_p = \bar{l}_p + \Delta l_p$, where the variation Δl_p is regarded as random.

The path delays τ_p are easily calculated for the lengths l_p, while the path gain h_p is obtained by using l_p instead of $\bar{l}_p$ in (8), which yields

$$h_p = \bar{h}_p \frac{1}{\sqrt{\left(1 + \dfrac{\Delta l_p}{\bar{l}_p}\right)^k \mathsf{a}_0^{\Delta l_p}}}. \tag{10}$$

Noting that for a typical system geometry we have that $\Delta l_p \ll \bar{l}_p$, and that $k \ll \bar{l}_p$, where $\bar{l}_p$ is expressed in meters, we proceed to make the following approximation:

$$\left(1 + \frac{\Delta l_p}{\bar{l}_p}\right)^k \approx 1 + k\frac{\Delta l_p}{\bar{l}_p} \approx \left(1 + \frac{k}{\bar{l}_p}\right)^{\Delta l_p}. \tag{11}$$

Fig. 3 illustrates the validity of this approximation for a given set of parameters.

With the approximation (11), the path gain can be expressed as

$$h_p \approx \bar{h}_p e^{-\xi_p \Delta l_p / 2} \tag{12}$$

where

$$\xi_p = \mathsf{a}_0 - 1 + \frac{k}{\bar{l}_p} \tag{13}$$

and the approximation follows from the fact that $\mathsf{a}_0 \approx 1$. Note that the linear approximation in (11) could also be used; however, we prefer the exponential one since it guarantees that the gain will be positive. Note also that if the path length variation (location uncertainty) can be modeled as Gaussian, the path gain will be log-normally distributed. We will use this notion in Section V, when we discuss the overall channel gain. The overall transfer function is now given as

$$H(f) = \bar{H}_0(f) \sum_p h_p e^{-j2\pi f \tau_p} \tag{14}$$

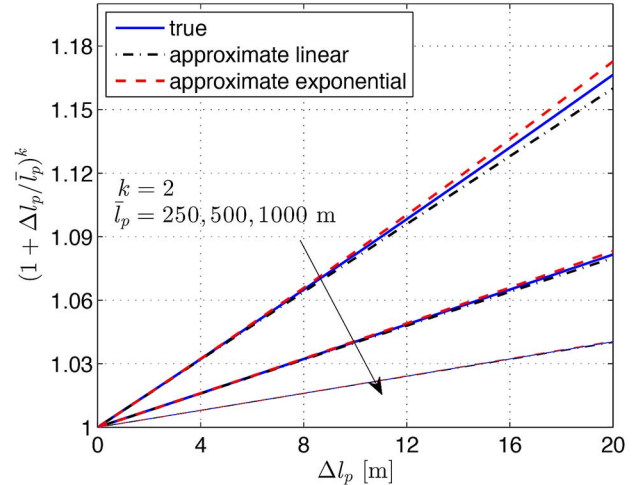where location uncertainty is captured by the large-scale parameters h_p and τ_p.

Fig. 3. Verifying the approximation (11). Both linear and exponential approximations yield error below 0.5% for the range of $\bar{l}_p$, Δl_p shown.

III. SMALL-SCALE CHANNEL CHARACTERIZATION

The channel transfer function (14) captures only the large-scale effects, i.e., it does not provide any information about fine-scale phenomena such as scattering. Scattering is a major contributor to signal variations that typically appear as random. A signal of frequency f undergoes scattering on rough surfaces and objects whose dimension is on the order of a few signal wavelengths $\lambda = c/f$. For example, the wavelength corresponding to an acoustic frequency component of 15 kHz is 0.1 m, hence the distances in question are called "small."

To model scattering in a UWA channel, let us focus on a single propagation path, say path p. So far, we have modeled this path as having the gain h_p and delay τ_p. However, if scattering occurs along this path, it is split into a number of micropaths

$$H(f) = \bar{H}_0(f) \sum_p \sum_i h_{p,i} e^{-j2\pi f \tau_{p,i}} \tag{15}$$

where $h_{p,i}$ are the intrapath gains, and $\tau_{p,i} = \tau_p + \delta\tau_{p,i}$ are the intrapath delays. Both the gains $h_{p,i}$ and the delays $\delta\tau_{p,i}$ are treated as random to account for random placement of scattering points within a scattering field. With this fact in mind, we define the small-scale fading coefficient as

$$\gamma_p(f) = \frac{1}{h_p} \sum_{i \geq 0} h_{p,i} e^{-j2\pi f \delta\tau_{p,i}} \tag{16}$$

so that the overall channel transfer function is expressed as

$$H(f) = \bar{H}_0(f) \sum_p h_p \gamma_p(f) e^{-j2\pi f \tau_p}. \tag{17}$$

A. Probability Density Function of the Small-Scale Coefficient $\gamma_p(f)$

Since the scattering points are separated by distances on the order of λ, the intrapath gains $h_{p,i}$ are likely to be similar, but the phases $2\pi f \delta\tau_{p,i}$, taken modulo 2π, can differ substantially between the intrapaths of the same path. These phase variations will, in turn, cause a significant variation in $\gamma_p(f)$.

Assuming that the constituent terms of the small-scale coefficient $\gamma_p(f)$ in (16) are independent and identically distributed,

the central limit theorem implies a complex Gaussian distribution for $\gamma_p(f)$ when the number of micropaths is sufficiently large (particularly, a good agreement is found already with ten micropaths). It is also possible to consider a situation in which there is a component whose delay is stable. In that case, the distortion is modeled by

$$\gamma_p(f) = \gamma_{p,0} + \sum_{i \geq 1} \gamma_{p,i} e^{-j2\pi f \delta \tau_{p,i}} \tag{18}$$

where $\gamma_{p,0}$ represents the relative coefficient of the stable path (whose $\delta\tau_{p,0} = 0$). In general, the coefficient $\gamma_p(f)$ is complex Gaussian with mean $\bar{\gamma}_p(f)$ and variance $2\sigma_p^2(f)$. This distribution is conditioned on both the large-scale parameters h_p and τ_p, and the small-scale path statistics $\bar{\gamma}_p(f)$ and $\sigma_p^2(f)$. While the former capture location uncertainty, the latter are influenced by the changing environmental conditions (e.g., surface roughness that changes with the wind/wave activity). Both sets of parameters can thus change over prolonged intervals of time.

The path statistics $\bar{\gamma}_p(f)$ and $\sigma_p^2(f)$ can be determined experimentally, or analytically if the distribution of the constituent terms in (16) is known. To illustrate an analytical approach, let us assume that the micropath amplitudes have the mean value μ_p and variance $\nu_p^2 \ll \mu_p^2$, and that the relative intrapath delays $\delta\tau_{p,i}$ are zero-mean Gaussian, with variance $\sigma_{\delta_p}^2$. Gaussian-distributed delays can, for instance, result from a Gaussian-distributed surface/bottom height. In that case, if we denote the surface and bottom variance by σ_s^2 and σ_b^2, respectively, we have that

$$\sigma_{\delta_p}^2 = \frac{1}{c^2}(2\sin\theta_p)^2[n_{sp}\sigma_s^2 + n_{bp}\sigma_b^2]. \tag{19}$$

The mean and variance of the scattering coefficients are then obtained as

$$\bar{\gamma}_p(f) = \mu_{p0} + \mu_p S_p \rho_p(f) \tag{20}$$
$$2\sigma_p^2(f) = \mu_p^2 S_p[1 - \rho_p^2(f)] + S_p\nu_p^2 \approx \mu_p^2 S_p[1 - \rho_p^2(f)] \tag{21}$$

where S_p is the number of intrapaths and

$$\rho_p(f) = E\{e^{-j2\pi f\delta\tau_{p,i}}\} = e^{-(2\pi f)^2\sigma_{\delta_p}^2/2}. \tag{22}$$

The last equality holds for Gaussian-distributed zero-mean intrapath delays. We note that the path statistics are determined by the function $\rho_p(f)$, whose value depends on the parameter $f\sigma_{\delta_p}$, i.e., the standard deviation of the micropath delay normalized by the signal wavelength. This function decays rapidly, falling below -10 dB for $f\sigma_{\delta_p} \geq 0.35$. In this regime, the independent real and imaginary components of the scattering coefficient have (approximately) equal variances, leading to the Ricean-distributed magnitude.

It is also worth noting that regardless of the distribution of $\delta\tau_{p,i}$, for high frequencies such that $f\sigma_{\delta_p} \gg 1$, the above model reduces to the one in which the phases $\phi_{p,i}$ are uniformly distributed. Such a model is typically used to describe radio communication channels.
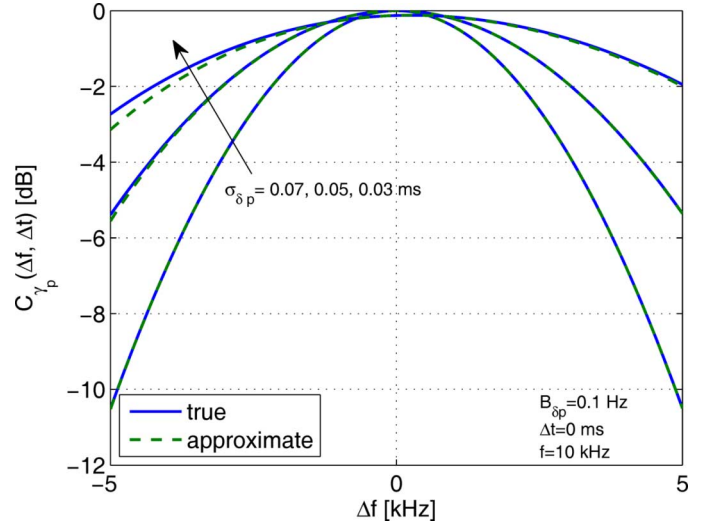

Fig. 4. Frequency-correlation function and its approximation, as defined in (24), for several values of the standard deviation $\sigma_{\delta p}$. The frequency f is set to 10 kHz, while Δf is varied.

B. Correlation Between Paths

Assuming that the scattering process is independent between different paths, i.e., that reflection points of different paths are sufficiently far apart, we have that

$$E\{\gamma_p(f)\gamma_q^*(f)\} = \bar{\gamma}_p(f)\bar{\gamma}_q(f) + \delta_{p,q}2\sigma_p^2(f). \tag{23}$$

Note that although the paths exhibit uncorrelated scattering, the above function is not zero in general, due to the nonzero mean values.

C. Correlation in the Frequency Domain

Frequency correlation of the small-scale path coefficients is described by the function $E\{\gamma_p(f + \Delta f, t)\gamma_q^*(f, t)\}$. To evaluate the frequency correlation, the probability density function (pdf) of the intrapath delays $\delta\tau_{p,i}$ has to be known. For the Gaussian-distributed delays with zero mean and variance $\sigma_{\delta_p}^2$, frequency correlation is obtained

$$E\{[\gamma_p(f + \Delta f) - \bar{\gamma}_p(f + \Delta f)][\gamma_p(f) - \bar{\gamma}_p(f)]^*\}$$
$$= \mu_p^2 S_p \rho_p(\Delta f)[1 - \rho_p(\sqrt{2f(f + \Delta f)})]$$
$$\approx \rho_p(\Delta f)2\sigma_p(f)\sigma_p(f + \Delta f) \tag{24}$$

where the approximation holds well (error below 4%) for $\sigma_{\delta_p} \geq 0.4/f_0$. Fig. 4 illustrates the frequency-correlation function and its approximation for a typical range of communication frequencies and several values of the standard deviation $\sigma_{\delta p}$. We note that depending upon the standard deviation of the path delays, there may be more or less correlation between the small-scale coefficients γ_p within the signal bandwidth. While the particular function of Fig. 4 pertains to Gaussian-distributed delays, one can expect a similar trend for a different distribution as well, i.e., one can expect the correlation to vary across a wide bandwidth. In our analysis of experimental data in Section VI, we will assume that full correlation exists across the signal bandwidth, i.e., that a single value γ_p suffices to describe small-scale effects. However, we note that this assumption may not always
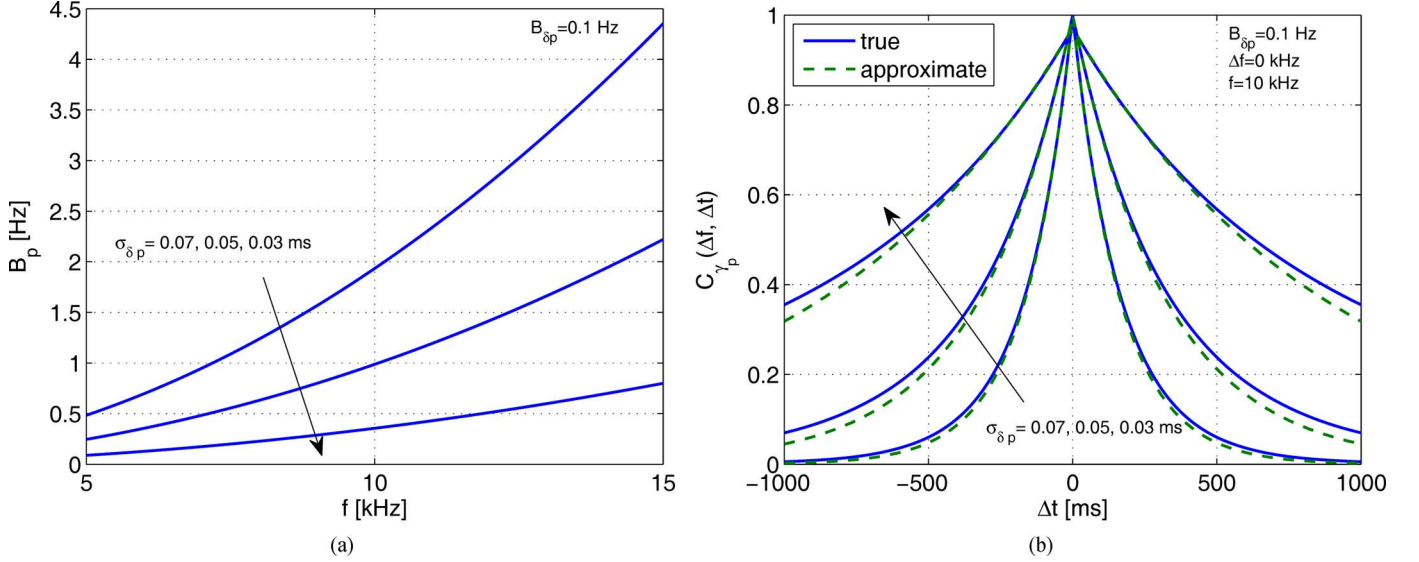
Fig. 5.   The functions (a) effective Doppler spread, (b) time correlation and its approximation, as defined in (26), for several values of the standard deviation $\sigma_{\delta p}$. The frequency f is set to 10 kHz, and $B_{\delta p} = 0.1$ Hz.

hold. Specifically, if $\sigma_{\delta p}$ is on the order of $1/f_0$, and the corresponding Ricean factor is low, there may be little correlation between $\gamma_p(f_0)$ and $\gamma_p(f_0 + B)$ in a wideband system. This fact may have serious implications on the performance of signal processing algorithms that rely on the assumption of frequency-invariant multipath coefficients.

D. Correlation in the Time Domain

Time correlation of the scattering coefficients is described by the function $E\{\gamma_p(f, t + \Delta t)\gamma_p^*(t)\}$. This function captures the effect of motion within the scattering field, which influences the coefficients $\gamma_p(f, t)$ through the time-varying micropath delays. To assess the time-correlation function, power spectral density (psd) of $\delta\tau_{p,i}(t)$ has to be known.

Without loss of generality, let us assume that the Gaussian-distributed delays $\delta\tau_{p,i}(t)$ obey a first-order autoregressive process (AR-1)

$$\delta\tau_{p,i}(t + \Delta t) = \alpha_{\delta p}\delta\tau_{p,i}(t) + w_{\delta p,i}(t) \qquad (25)$$

where

$$w_{\delta p,i}(t) \sim \mathcal{N}(0, \sigma_{\delta p}^2(1 - \alpha_{\delta p}^2))$$
$$\alpha_{\delta p} = e^{-\pi B_{\delta p}\Delta t}$$

and $B_{\delta p}$ is the 3-dB width of the psd of $\delta\tau_{p,i}(t)$. The above relationship is not a binding one; it simply states that two values of delay are expected to look more alike if they are more closely spaced in time, i.e., that one does not expect the delays to vary completely erratically, but to show some coherence. The time-correlation function is then obtained as

$$E\{[\gamma_p(f, t + \Delta t) - \bar{\gamma}_p(f)][\gamma_p(f, t) - \bar{\gamma}_p(f)]^*\}$$
$$= \mu_p^2 S_p e^{-(1-\alpha_{\delta p})(2\pi f)^2\sigma_{\delta p}^2}[1 - e^{-\alpha_{\delta p}(2\pi f)^2\sigma_{\delta p}^2}]$$
$$\approx 2\sigma_p^2(f)e^{-\pi B_p(f)\Delta t} \qquad (26)$$

where the approximation holds for $\Delta t \ll 1/B_{\delta p}$, and we have defined

$$B_p(f) = (2\pi f\sigma_{\delta p})^2 B_{\delta p} \qquad (27)$$

as the effective Doppler bandwidth (Doppler spread) of the path coefficient $\gamma_p(f, t)$. Fig. 5 illustrates the effective Doppler spread, the time-correlation function, and its approximation. As one can expect, stronger temporal correlation is observed for lower values of the standard deviation $\sigma_{\delta p}$.

The complete autocorrelation function of the process $\gamma_p(f, t)$ can also be expressed in closed form. Using the relationships (24) and (26), we obtain a generalization

$$E\{[\gamma_p(f_1, t + \Delta t) - \bar{\gamma}_p(f_1)][\gamma_p(f_2, t) - \bar{\gamma}_p(f_2)]^*\}$$
$$= \mu_p^2 S_p e^{-(2\pi(f_1 - f_2))^2\sigma_{\delta p}^2/2}$$
$$\times e^{-(1-\alpha_{\delta p})(2\pi f_1)(2\pi f_2)\sigma_{\delta p}^2}[1 - \rho_p(\sqrt{2\alpha_{\delta p}f_1 f_2})]$$
$$\approx \rho_p(f_1 - f_2)e^{-\pi B_p(f_{1,2})\Delta t}2\sigma_p(f_1)\sigma_p(f_2) \qquad (28)$$

where $f_{1,2}$ stands for either of the two frequencies f_1 or f_2 within the signal bandwidth. Setting $f_1 = f + \Delta f$ and $f_2 = f$, the above expression defines the function $C_{\gamma_p}(\Delta f, \Delta t)$, whose special forms obtained for $\Delta t = 0$ and for $\Delta f = 0$ in (24) and (26) were illustrated in Figs. 4 and 5, respectively.[1]

E. Statistically Equivalent Model for $\gamma_p(f, t)$

Let us define an auxiliary AR-1 process

$$\Delta\gamma_p(f, t + \Delta t) = \alpha_p(f)\Delta\gamma_p(f, t) + w_p(f, t)$$
$$\gamma_p'(f, t + \Delta t) = \bar{\gamma}_p(f) + \Delta\gamma_p(f, t + \Delta t) \qquad (29)$$

where $w_p(t)$ is a complex Gaussian random process

$$w_p(t) \sim \mathcal{CN}(0, 2\sigma_p^2(f)(1 - \alpha_p^2(f)))$$

[1]Note that this function depends on f as well, although we explicitly denote only the dependence on Δf.

where $\alpha_p(f) = e^{-\pi B_p(f)\Delta t}$. Process (29) is characterized by a Gaussian pdf

$$\gamma'_p(f,t) \sim \mathcal{CN}(\bar{\gamma}_p(f), 2\sigma_p^2(f))$$

and an autocovariance function

$$E\{\Delta\gamma_p(f,t+\Delta t)\Delta\gamma_p^*(f,t)\} = 2\sigma_p^2(f)e^{-\pi B_p(f)\Delta t}.$$

Since its pdf and psd coincide with those of the process $\gamma_p(f,t)$, the two processes are *statistically* equivalent.

The significance of the auxiliary process $\Delta\gamma_p(f,t)$ is that it can easily be generated in computer simulation. To do so, a single recursive operation needs to be applied to a Gaussian input, as specified by (29).

To develop a full channel simulator, however, frequency correlation needs to be embedded into the process $\Delta\gamma_p(f,t)$. To this end, let us discretize the frequency axis in steps of Δf_s and the time axis in steps of Δt_s, and let us define the vector

$$\boldsymbol{\Delta\gamma}_p[n] = [\Delta\gamma_p(f_0, t_0 + n\Delta t_s), \Delta\gamma_p(f_1, t_0 + n\Delta t_s), \ldots]^T.$$

Let us also define the matrix $\mathbf{A}_p = \text{diag}[\alpha_p(f_k)]$, where $\alpha_p(f_k) = e^{-\pi B_p(f_k)\Delta t_s}$.

We are now in a position to specify an AR-1 process as follows. Starting with some $\boldsymbol{\Delta\gamma}[0]$, e.g., an all-zero vector, generate

$$\boldsymbol{\Delta\gamma}_p[n+1] = \mathbf{A}_p\boldsymbol{\Delta\gamma}_p[n] + \mathbf{w}_p[n], \qquad n = 0, 1, \ldots \quad (30)$$

where

$$\mathbf{w}_p[n] \sim \mathcal{CN}(0, \mathbf{W}_p)$$

and

$$[\mathbf{W}_p]_{k,l} = [1 - \alpha_p(f_k)\alpha_p(f_l)]\rho_p(f_k - f_l)2\sigma_p(f_k)\sigma_p(f_l).$$

This particular choice of the process noise covariance matrix $\mathbf{W}_p$ ensures the desired frequency correlation

$$E\{\Delta\gamma_p(f_k,t)\Delta\gamma_p^*(f_l,t)\} = \rho_p(f_k - f_l)2\sigma_p(f_k)\sigma_p(f_l)$$

as well as the complete correlation given by (28).

The above model retains computational simplicity, thus offering an appealing platform for channel simulation. After executing the recursion (30) over a time interval of interest and for frequencies corresponding to the desired signal bandwidth, all that remains to be done is to add the mean values $\bar{\gamma}_p(f_k)$ to the so-obtained coefficients $\Delta\gamma_p(f_k, n\Delta t_s)$. The result is a discrete-time discrete-frequency random process $\gamma'_p(f,t)$ whose statistical properties are equivalent to those of the sampled process $\gamma_p(f,t)$.

We emphasize that a channel simulator does *not* yield an exact replica of an actual channel because 1) it is only *statistically* equivalent to the process $\gamma_p(f,t)$ as we have defined it; and 2) our definition of the process $\gamma_p(f,t)$ is itself incomplete. Namely, while it takes into account rough surface scattering, it does not take into account the particular shape of the surface or

the effect of breaking waves which inject bubbles into the water column. Both of these effects can additionally alter the signal, or even completely occlude the surface [18], [19]. The above model should thus be regarded as a first step toward assessing the small-scale variations. Imperfect as it may be, this model offers a simulation platform that captures some of the acoustic channel effects in a *computationally efficient* manner.

IV. MOTION-INDUCED DOPPLER SHIFTING

Motion of the transmitter/receiver or any reflection points in the channel leads to time-varying path delays τ_p. Focusing on the small-scale phenomena, we are interested in variations that occur over short intervals of time (e.g., subsecond intervals). During such intervals, say $[t_0, t_0 + T]$, it is reasonable to assume that any motion occurs at a constant velocity, i.e., that it is only the velocity and not acceleration that matters. When that is the case, the path delays are modeled as $\tau_p(t) = \tau_p - a_p t$ where $t \in [0, T]$ and $a_p = v_p/c$ is the Doppler factor corresponding to velocity v_p.[2] Note that the Doppler factors a_p may (and likely will) vary with time and a more general quasi-stationary model can be introduced to address this fact. Specifically, one may wish to divide the time axis into consecutive intervals of constant velocity, and associate a Doppler scaling factor $a_p(n)$ with the nth interval. We will keep this fact in mind, but drop time indexing for simplicity where appropriate.

At least three types of motion influence the Doppler factor: 1) unintentional transmitter/receiver motion, i.e., *drifting*, which gives rise to a Doppler scaling factor a_{dp}; 2) intentional transmitter/receiver motion, i.e., *vehicular* motion, which gives rise to a_{vp}; and 3) waves, i.e., *surface* motion, which gives rise to a_{sp}. If the Doppler factors corresponding to each of these types of motion are fixed, the corresponding Doppler shift is always the same. On the contrary, if the Doppler factors change randomly from one time interval to another, so do the shifts. The resulting effect is that of random Doppler shifting or Doppler spreading. The overall small-scale path coefficient can now be defined as

$$\tilde{\gamma}_p(f,t) = \gamma_p(f,t)e^{j2\pi a_p ft}. \quad (31)$$

To characterize Doppler spreading, we focus on the autocorrelation function of the random process $e^{j2\pi a_p ft}$, i.e., $E\{e^{j2\pi a_p f\Delta t}\}$. Assuming independence between various factors contributing to motion, we have that

$$R_p(\Delta t) = E\{e^{j2\pi f a_{dp}\Delta t}\}E\{e^{j2\pi f a_{vp}\Delta t}\}E\{e^{j2\pi f a_{sp}\Delta t}\}. \quad (32)$$

Should any one of these components be regarded as deterministic, its expectation is dropped.

To characterize the drifting component, we assume that the transmitter and the receiver drift at velocities v_{td} and v_{rd} in directions θ_{td} and θ_{rd} with respect to horizontal pointed toward each other. The relative speed, projected onto the pth path is

$$v_{dp} = v_{td}\cos(\theta_p - \theta_{td}) - v_{rd}\cos(\theta_p + \theta_{rd}) \quad (33)$$

[2]It is also possible to account for a path-dependent propagation speed.

and the corresponding Doppler factor is $a_{dp} = v_{dp}/c$. If the transmitter and the receiver drift in random directions, then $E\{e^{j2\pi f a_{dp}\Delta t}\}$ involves averaging over θ_{td} and θ_{rd}. Assuming that drifting is equally likely in any direction, and that it occurs independently for the transmitter and the receiver

$$
\begin{aligned}
E\{e^{j2\pi f a_{dp}\Delta t}\} &= E\{e^{j2\pi(v_{td}/c)f\cos(\theta_p - \theta_{td})\Delta t}\} \\
&\quad \times E\{e^{j2\pi(v_{rd}/c)f\cos(\pi+\theta_p+\theta_{rd})\Delta t}\} \\
&= \frac{1}{2\pi}\int_0^{2\pi} e^{j2\pi(v_{td}/c)f\cos(\theta'_{td})\Delta t}d\theta'_{td} \\
&\quad \times \frac{1}{2\pi}\int_0^{2\pi} e^{j2\pi(v_{rd}/c)f\cos(\theta'_{rd})\Delta t}d\theta'_{rd} \\
&= J_0\left(2\pi\frac{v_{td}}{c}f\Delta t\right) J_0\left(2\pi\frac{v_{rd}}{c}f\Delta t\right) \quad (34)
\end{aligned}
$$

where $\theta'_{td} = \theta_p - \theta_{td}$ and $\theta'_{rd} = \pi + \theta_p + \theta_{rd}$ are uniformly distributed on the interval $[-\pi, \pi]$, and $J_0(\cdot)$ is the Bessel function of the first kind and order zero. Assuming $v_{td} = v_{rd} = v_d$ and $a_d = v_d/c$, the above expression reduces to $J_0^2(2\pi a_d f\Delta t)$.

Vehicular component of the Doppler effect is obtained similarly, except that those components of motion that can be estimated and compensated by synchronization are not to be regarded as part of the channel distortion. Hence, we regard $a_{vp} = v_{vp}/c$ as the *residual* Doppler factor after initial synchronization. For example, if synchronization compensates for the predominant Doppler factor corresponding to the projection of the transmitter/receiver intentional velocity onto the reference path $p = 0$, the effective Doppler factor is

$$
\begin{aligned}
a_{vp} &= \frac{1}{c}\Big[[v_{tv}\cos(\theta_p - \theta_{tv}) - v_{rv}\cos(\theta_p + \theta_{rv})] \\
&\quad - [v_{tv}\cos(\theta_0 - \theta_{tv}) - v_{rv}\cos(\theta_0 + \theta_{rv})]\Big] \\
&= \frac{1}{c}\Bigg[v_{tv}\left[-2\sin\left(\frac{\theta_p + \theta_0 - 2\theta_{tv}}{2}\right)\sin\left(\frac{\theta_p - \theta_0}{2}\right)\right] \\
&\quad + v_{rv}\left[2\sin\left(\frac{\theta_p + \theta_0 + 2\theta_{rv}}{2}\right)\sin\left(\frac{\theta_p - \theta_0}{2}\right)\right]\Bigg].
\end{aligned}
$$
$$(35)$$

Assuming that the transmitter/receiver motion is equally likely in any direction $\theta_{tv/rv}$, the autocorrelation function corresponding to vehicular motion is

$$
\begin{aligned}
E\{e^{j2\pi f a_{vp}\Delta t}\} &= J_0\left(2\pi\frac{2v_{tv}\sin\left(\frac{\theta_p - \theta_0}{2}\right)}{c}f\Delta t\right) \\
&\quad \times J_0\left(2\pi\frac{2v_{rv}\sin\left(\frac{\theta_p - \theta_0}{2}\right)}{c}f\Delta t\right).
\end{aligned}
$$
$$(36)$$

Finally, to assess the surface component, let us focus on waves that cause a point on the surface to move up and down

creating a displacement that varies sinusoidally in time, with amplitude A_w and frequency f_w. Note that we are accounting only for the vertical surface motion, and not for the horizontal group velocity of the waves or the effect of an inclined surface (a study on scattering from inclined waves can be found in [4]). A signal impinging upon the jth reflection point along the pth path catches it in a random phase, i.e., at vertical velocity $v_w\sin(\psi_{p,j} + 2\pi f_w t)$, where $\psi_{p,j} \sim \mathcal{U}[-\pi, \pi]$, and $v_w = 2\pi f_w A_w$. Projections of this velocity onto the pth path, summed over all surface reflection points, yield

$$
v_{sp} = 2v_w\sin\theta_p\sum_{j=1}^{n_{sp}}\sin(\psi_{p,j} + 2\pi f_w t). \quad (37)
$$

Assuming that reflection points are sufficiently far apart such that $\psi_{p,j}$ are independent, time correlation is obtained by taking the expectation over $a_{sp} = v_{sp}/c$ with the angles $\psi_{p,j}$ uniformly distributed over 2π. The result is

$$
E\{e^{j2\pi f a_{sp}\Delta t}\} = [J_0(2\pi a_{wp}f\Delta t)]^{n_{sp}} \quad (38)
$$

where $a_{wp} = 2v_w\sin\theta_p/c$ and n_{sp} is the number of surface encounters along path p.

Putting together (26) and (34)–(38), the complete autocorrelation function of the overall small-scale coefficient $\tilde{\gamma}_p(f, t)$ is obtained as

$$
\begin{aligned}
R_{\tilde{\gamma}_p}(\Delta t) &= \left[\bar{\gamma}_p^2(f) + 2\sigma_p^2(f)e^{-\pi B_p(f)\Delta t}\right]J_0^2(2\pi a_d f\Delta t) \\
&\quad \times J_0\left(2\pi\frac{2v_{tv}\sin\left(\frac{\theta_p - \theta_0}{2}\right)}{c}f\Delta t\right) \\
&\quad \times J_0\left(2\pi\frac{2v_{rv}\sin\left(\frac{\theta_p - \theta_0}{2}\right)}{c}f\Delta t\right) \\
&\quad \times \left[J_0\left(2\pi\frac{2v_w\sin\theta_p}{c}f\Delta t\right)\right]^{n_{sp}}. \quad (39)
\end{aligned}
$$

This function exhibits an overall Bessel-like behavior, dampened by the exponentially decaying correlation of the scattering coefficient γ_p [first term in (39)]. Fig. 6 shows $R_{\tilde{\gamma}_p}(\Delta t)$ for two different scenarios: one in which surface motion alone is taken into account, and another in which surface and drifting motions are considered. In both scenarios, the first zero crossing of the overall Bessel-like correlation function, which indicates the coherence time, is determined by the maximum of the surface or drifting velocities and the number of surface reflections. It is also worth noting that the main lobe of the surface component, whose behavior is dictated by the Doppler factor a_{wp}, narrows with each additional surface encounter. This fact implies that each surface encounter adds to the overall time variation of the signal, which is intuitively satisfying. Most notably, as we will see in Section VI, experimental results demonstrate similar behavior. The correlation function (39), although obtained analytically under a number of modeling assumptions, thus becomes helpful in explaining experimental observations.
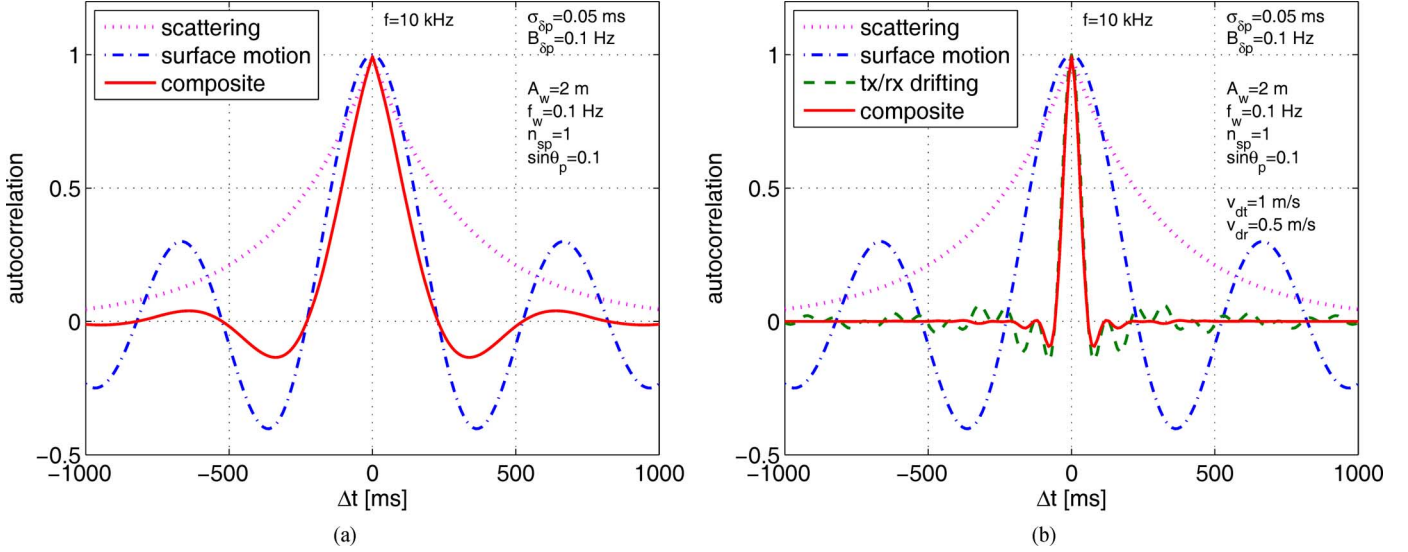
Fig. 6. Autocorrelation of the small-scale coefficient $\tilde{\gamma}_p$ for (a) surface motion and (b) surface and drifting motions.

V. THE CHANNEL GAIN

So far, we have developed a model that represents the time-varying channel transfer function as

$$H(f,t) = \bar{H}_0 \sum_p h_p \tilde{\gamma}_p(f,t) e^{-j2\pi f \tau_p} \qquad (40)$$

where $\tilde{\gamma}_p(f,t) = \gamma_p(f,t) e^{j2\pi a_p f t}$ as in (31). This function completely describes the channel for a given set of large-scale parameters h_p and τ_p, the path statistics $\bar{\gamma}_p(f), \sigma_p^2(f)$, and the Doppler scaling factors a_p. We recall that these parameters may also vary with time, each at its own rate. The different time scales at which these parameters vary give rise to the definition of different figures of merit for a communication system design.

An important figure of merit for communication systems is the overall channel gain, i.e., the overall energy, or power, contained in the channel response at a given time. We define the instantaneous channel gain for a system operating in the frequency range $[f_0, f_0 + B]$ as

$$\tilde{G}(t) = \frac{1}{B} \int_{f_0}^{f_0+B} |H(f,t)|^2 df \qquad (41)$$

and the corresponding locally averaged gain as

$$G = E_{\tilde{\gamma}}\left\{ \tilde{G}(t) \right\}. \qquad (42)$$

If the bandwidth is large enough such that all multipath components are clearly resolvable, the gain will be dominated by individual multipath components

$$G = \sum_p G_p h_p^2 \qquad (43)$$

where

$$G_p = \frac{1}{B} \int_{f_0}^{f_0+B} \bar{H}_0^2(f)[\bar{\gamma}_p^2(f) + 2\sigma_p^2(f)] df. \qquad (44)$$

We refer to the gain G as the large-scale gain, and note that it depends on both the path coefficients h_p and the path statistics $\bar{\gamma}_p(f), \sigma_p^2(f)$. The large-scale gain is thus a random variable, whose statistics are determined by those of the path gains h_p. The path gains, and, consequently, the channel gain, can also be modeled as random processes, so as to explicitly take into account their time dependence $h_p(t)$. The gain will then become a random process itself, which we denote as $G(t)$. We emphasize that the time scales involved in this type of modeling are larger than those used for small-scale effects, i.e., that $h_p(t)$ changes more slowly than $\gamma_p(f,t)$. Finally, we note that the path *statistics* can also change with time, as dictated by the environmental conditions. These changes are likely to occur on even longer time scales.

The distribution of the gain can be assessed analytically if the distribution of the path gains is known. Recalling the model (12), we have that

$$G(t) = \sum_p G_p \bar{h}_p^2 e^{-\xi_p \Delta l_p(t)}. \qquad (45)$$

Assuming that the path lengths are Gaussian distributed with mean $\bar{l}_p$ and variance $\sigma_{l_p}^2$, the gain is a sum of log-normally distributed random processes, which can be modeled as a log-normal process itself (see [22] and the references therein). The mean and variance of the approximate log-normal sum can be calculated using the Fenton–Wilkinson method described in [22] as

$$\bar{G} = \sum_p G_p \bar{h}_p^2 e^{\xi_p^2 \sigma_{l_p}^2 / 2}$$

$$\sigma_G^2 = \sum_p G_p^2 \bar{h}_p^4 e^{\xi_p^2 \sigma_{l_p}^2} (e^{\xi_p^2 \sigma_{l_p}^2} - 1). \qquad (46)$$

Thus, in the case of independent and small zero-mean Gaussian path length displacements, the gain behaves approximately as log-normally distributed. On the decibel scale, we have that

$$g(t) = \bar{g} + \Delta g(t) \qquad (47)$$

Algorithm 1: Channel simulator

---

1 Initialization: set $\bar{h}_p, \bar{\tau}_p, \sigma_{\delta p}^2$ *Use Bellhop or similar tracing method for a specified system geometry, sound speed profile; use environmental statistics*

2 **for** each realization of the large-scale process **do**

3   set h_p, τ_p

4   **for** each realization of the small-scale process on an observation interval $t \in [0, T_{obs}]$ **do**

5   **for** $p = 1, \ldots, P$ **do**

6         $\gamma_p(f,t) = \frac{1}{h_p} \sum_i h_{p,i} e^{-j2\pi f \delta \tau_{p,i}(t)}$ *Generate directly as indicated, or use Eq. (30)*

7         $\tilde{\gamma}_p(f,t) = \gamma_p(f,t) e^{j2\pi a_p f t}$ *Add motion-induced Doppler; allow for time-varying Doppler scaling factor if so desired*

8      $H(f,t) = \bar{H}_0(f) \sum_p h_p \tilde{\gamma}_p(f,t) e^{-j2\pi f \tau_p}$ output: channel transfer function

9      $\tilde{G}(t) = \frac{1}{B} \int_{f_0}^{f_0+B} |H(f,t)|^2 df$ output: instantaneous channel gain

10 $G = E_{\tilde{\gamma}} \left\{ \tilde{G}(t) \right\}$ output: locally-averaged gain (ensemble average over small-scale realizations)

---

where

$$\bar{g} = 10 \left[2 \log_{10} \bar{G} - \frac{1}{2} \log_{10}(\bar{G}^2 + \sigma_G^2) \right]$$

and $\Delta g(t)$ is zero-mean Gaussian with variance

$$\sigma_g^2 = 10^2 (\log_{10} e) \left[\log_{10}(\bar{G}^2 + \sigma_G^2) - 2 \log_{10} \bar{G} \right].$$

The model (47) holds for a fixed channel geometry, which defines the nominal attenuation for the transmission distance $d = \bar{l}_0$. If the nominal geometry changes, e.g., due to vehicular motion over a period of time, $\bar{g}$ will change accordingly. Specifically, $\bar{g}$ is expected to maintain a log-distance relationship

$$\bar{g}(d) = g_0 - k_0 10 \log \frac{d}{d_{\text{ref}}} \tag{48}$$

where d_{ref} is a reference distance, e.g., 1 m. The constant g_0 and the effective spreading factor or path loss exponent k_0, which depends on operational frequency, can be estimated from ensemble averages of the gains obtained at varying distances [9]. Experimental data, as well as numerical simulations, also show that the variance σ_g^2 is independent of the distance, and is inversely proportional to the bandwidth B. To highlight this dependence on distance, we rewrite (47) as

$$g(d,t) = \bar{g}(d) + \Delta g(t). \tag{49}$$

Time-correlation properties of the large-scale gain $g(d,t)$ depend on the actual motion pattern, and are best left to specific examples. Experimental observations, which will be discussed in Section VI, seem to attest to an exponential autocorrelation of the gain Δg, which indicates the possibility to model the gain as an autoregressive process. If the time-varying gain in an actual channel can indeed be modeled as a simple AR process (of order 1 or more), this fact has significant implications on the use of adaptive power control. Namely, it implies the possibility to *predict* the gain a few seconds ahead, thus allowing the transmitter to cater to the receiver's needs at the time of signal arrival, rather than simply acting upon outdated information about the

receiver's state. A study on the prediction of the UWA channel impulse response was conducted in [21].

Algorithm 1 summarizes the steps for designing an underwater channel simulator based on the model described throughout the paper. We emphasize that this simulator is designed to address multipath, rough surface scattering, motion-induced Doppler, and large-scale variation in the channel geometry; however, it does not take into account the surface curvature, or the effect of breaking waves which add extensive complexity to the model. In addition, it assumes Gaussian-distributed intrapath delays of the scattered paths. Hence, we regard this simulator as a first approximation for computationally efficient modeling of a class of underwater acoustic channels.

VI. EXPERIMENTAL RESULTS

We present experimental data collected during four experiments. Table I lists the operational frequency range used in each experiment (B), the distance between the transmitter and the receiver (d), the water depth (h_w), and the transmitter/receiver height above the bottom $(h_{tx/rx})$. In the first three experiments, the probing signals were custom designed, transmitted over the channel, and recorded for subsequent offline processing. The probing signals were pseudonoise (PN) sequences, periodically repeated and binary phase-shift keying (BPSK) modulated onto the center frequency at full rate. In the fourth experiment, frequency-modulation (FM) sweep signals were transmitted and received by the Woods Hole Oceanographic Institution (WHOI, Woods Hole, MA, USA) micromodem [23]. Only the received signal strength, and not the full channel response, is available from this experiment.

The first experiment, called the Surface Processes and Acoustic Communications Experiment (SPACE) was conducted near the coast of Martha's Vineyard in Massachusetts, USA, in fall 2008. The carrier frequency was 13 kHz and the transmission rate was 6.5 kb/s. The signal was transmitted for 3 min every 2 h. We refer to the active 3-min interval of each 2-h period as one epoch. The experiment lasted for 15 days. The water depth was 10 m, and the transmitter and the receiver were

fixed at 4 and 2 m above the seafloor, respectively. Receivers located at distances of 60, 200, and 1000 m from the transmitter recorded the signals.

The second experiment, Mobile Acoustic Communications Experiment (MACE), was conducted in the Atlantic Ocean about 100 miles south of Martha's Vineyard in summer 2010. The receiver was suspended at the depth of 40 m and the transmitter was towed at the depth of 50–60 m. The water depth was approximately 100 m, and the distance varied between 500 m and 4 km. The carrier frequency was 13 kHz, and the signals were transmitted continuously at 5 kb/s.

The third experiment, known as the Kauai AComms Multidisciplinary University Research Initiative (MURI) (KAM), was conducted in July 2011 off the coast of Kauai Island, HI, USA. The transmitter and the receiver were deployed approximately midway in 100-m water and were 3 km apart. The signals were modulated onto the carrier of 13 kHz and transmitted at the rate of 6.5 kb/s during 9-min epochs every 2 h.

Finally, the fourth experiment, called the Pacific Storm (PS) experiment, was conducted on the submerged portion of San Andreas Fault off the coast of Northern California in September 2010. During this experiment, data packets of length 3 s were repeatedly transmitted every 5 s from an autonomous underwater vehicle (AUV) to a surface ship. The signals occupied 4 kHz of bandwidth around a center frequency of 10 kHz. The AUV was moving at about 3 m above the bottom, at a depth of approximately 130 m. The transmission distance varied from 200 m to 1 km. In this experiment, the signals were automatically processed by the acoustic modems mounted on the two ends of the link. The received signal strength was recorded once a second.

A. Small-Scale Analysis

The signals from the SPACE, MACE, and KAM experiments were used to assess the small-scale channel behavior. The signals were first resampled based on the received packet length to compensate for the motion-induced time scaling and frequency shifting which can be modeled by a rough Doppler factor. Resampling was notably necessary for the MACE data, where the transmitter moved at about 1 m/s, creating a raw Doppler rate on the order of 10^{-3}. Fine Doppler compensation was then carried out using a combined recursive least squares (RLS) estimator and a second-order phase-locked loop (PLL). Once these steps were completed, the orthogonal matching pursuit (OMP) algorithm [24] was used for channel estimation. This algorithm is commonly used for estimation of UWA channels as it outperforms conventional least squares methods when the channel is sparse. The resulting estimate of the baseband channel response was then used to extract the path gains.

Figs. 7–9 show the results obtained for the three experiments. Each figure shows an ensemble of channel responses (magnitude), histograms of several selected paths, and their autocorrelation functions. The channel responses are shown over the duration of 1 min at a resolution of 1 b. Several local maxima over the delay axis are visible in the figures, indicating channel taps over which the impulse response is the strongest. Physical path delays corresponding to the nominal channel geometry are marked by arrows and labeled as s, b, sb, $s2b$, etc., referring to

	B [kHz]	d [km]	h_w [m]	h_{tx} [m]	h_{rx} [m]
SPACE	8–17	0.06, 0.2, 1	10	4	2
MACE	10.5–15.5	0.5–4	100	45	60
KAM	8.5–17.5	3	103	58	59
PS	8–12	0.2–1	130	3	$\sim$130

surface, bottom, surface–bottom, surface–bottom–surface, etc., reflections.

The observed path delays deviate from the nominal ones because of location uncertainty, motion-induced Doppler effect, and intrapath delay spreading. In addition, time variability of the channel imparts a slowly varying mean onto each path. Also, if the geometry is such that two paths have similar lengths, path merging will occur, i.e., their arrival times will be too close to be distinguished given the delay resolution (finite bandwidth) of the system. Path spreading, which is a consequence of both the micropath dispersion and bandwidth limitation, may occur uniformly at a tractable rate, as in the path labeled p_0 in the KAM experiment, or an intractable one, as in the path labeled p_{bs}. To take into account the effect of all contributing taps, whenever the phase information is not needed, several adjacent taps are combined in a root mean square (rms) fashion to form the absolute value of a given path gain. Slow variation of the mean, which is a consequence of the changing $h_p(t)$, is then removed. For example, such variation is evident in the path p_s of the MACE experiment. In this case, to extract the absolute value of the small-scale factor $\gamma_p(t)$, the slowly varying window average of the observed process $|h_p(t)\gamma_p(t)|$ is removed. When the phase information is not to be neglected, the signal statistics are estimated over shorter time intervals, i.e., several seconds.

The histograms shown in Figs. 7–9 are those of the estimated $|\gamma_p(t)|$ for several selected paths, along with a theoretical Ricean curve. The magnitude $|\gamma_p(t)|$ is estimated as the rms of the maximum tap and its significant neighbors, whose time-varying mean is removed. The stationarity of the data was tested using the Phillips–Perron test [25]. The null hypothesis that the estimated time series has a unit root, which gives rise to nonstationarity, was rejected for all data sets. The maximum-likelihood method is used to estimate the parameters of the fitted Ricean curve. We have also measured the variance on individual segments of data (sliding window average, after removing the time-varying mean) and have found it to remain constant. This observation also confirms the stationarity of the data in the wide sense. The conditional Ricean distribution (conditioned on the slowly varying mean) appears to provide a good fit in all three experiments. The 95% confidence intervals of the histogram bars are plotted. For almost every bar, the Ricean fit falls inside the confidence interval, which can be interpreted as a qualitative measure of goodness of the fits. To further quantify the goodness of fit, the Jensen–Shannon (JS) divergence [26] was used. The JS divergence is a symmetric measure of the difference between two distributions P and Q, and is defined as

$$D_{\text{JS}}(P\|Q) = \frac{1}{2}D_{\text{KL}}(P\|M) + \frac{1}{2}D_{\text{KL}}(Q\|M) \qquad (50)$$
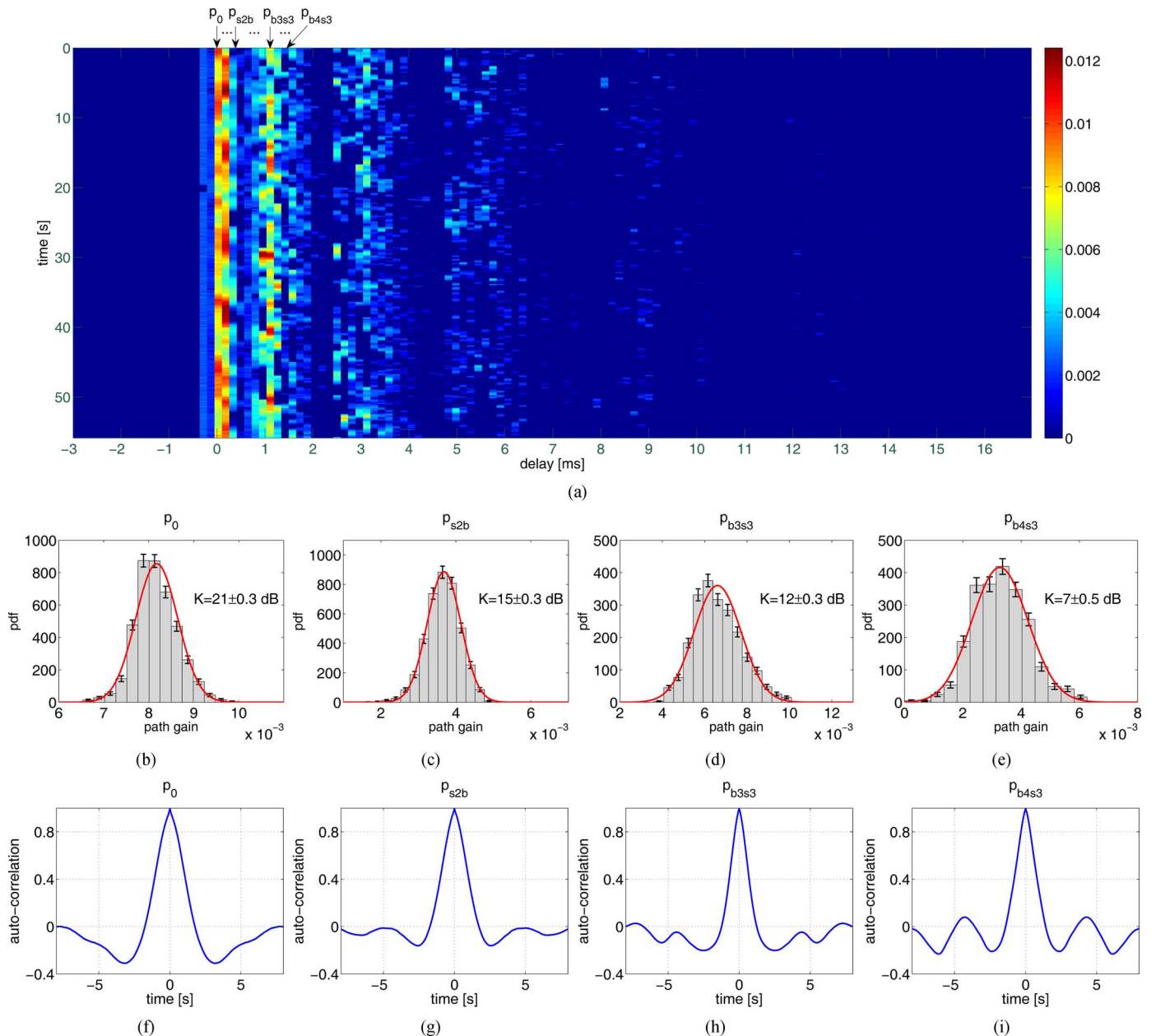
Fig. 7. SPACE experiment: (a) time evolution of the magnitude baseband impulse response; (b)–(e) histograms of selected path magnitudes; and (f)–(i) time-correlation functions.

where $M = (P + Q)/2$ and $D_{KL}(P \| Q) = \sum_i P_i \ln(P_i/Q_i)$ denotes the Kullback–Leibler (KL) divergence of the fit Q from the distribution P. Table II lists the values of the JS divergence between the estimated histograms and the fitted Ricean distributions (gray rows) for the different paths analyzed in Figs. 7–9. The JS divergence values for a fitted Rayleigh distribution are also listed in the table (white rows). Ricean distribution provides a better fit for all path gain data sets. The Ricean K-factor is indicated in the figures along with its 95% confidence interval. Its value for the direct path ($p = 0$) is greater than that of the other paths, indicating a stable arrival as there is no surface dispersion.

Finally, the time-domain autocorrelation functions of the path coefficients are plotted. We note a remarkable similarity with the theoretical results of Section IV and the Bessel-like functions developed there. For all three experiments, the autocor-

relations corresponding to the direct path show less fluctuation and a higher coherence time. All other paths show Bessel-type autocorrelation, and, as noted in Section III, Doppler bandwidth that increases with the number of surface encounters.

B. Large-Scale Analysis

Fig. 10 summarizes the results of large-scale data analysis. This analysis targets the window averaged channel gain observed over longer periods of time. A rectangular window of length 2 s is used. Included in the figure are the results of all four experiments. The figure shows four columns, each corresponding to one of the experiments. Each column contains four plots, showing the gain g versus time (for the duration of the experiment), the gain versus distance, the histogram of the gain deviation Δg, and its autocorrelation.
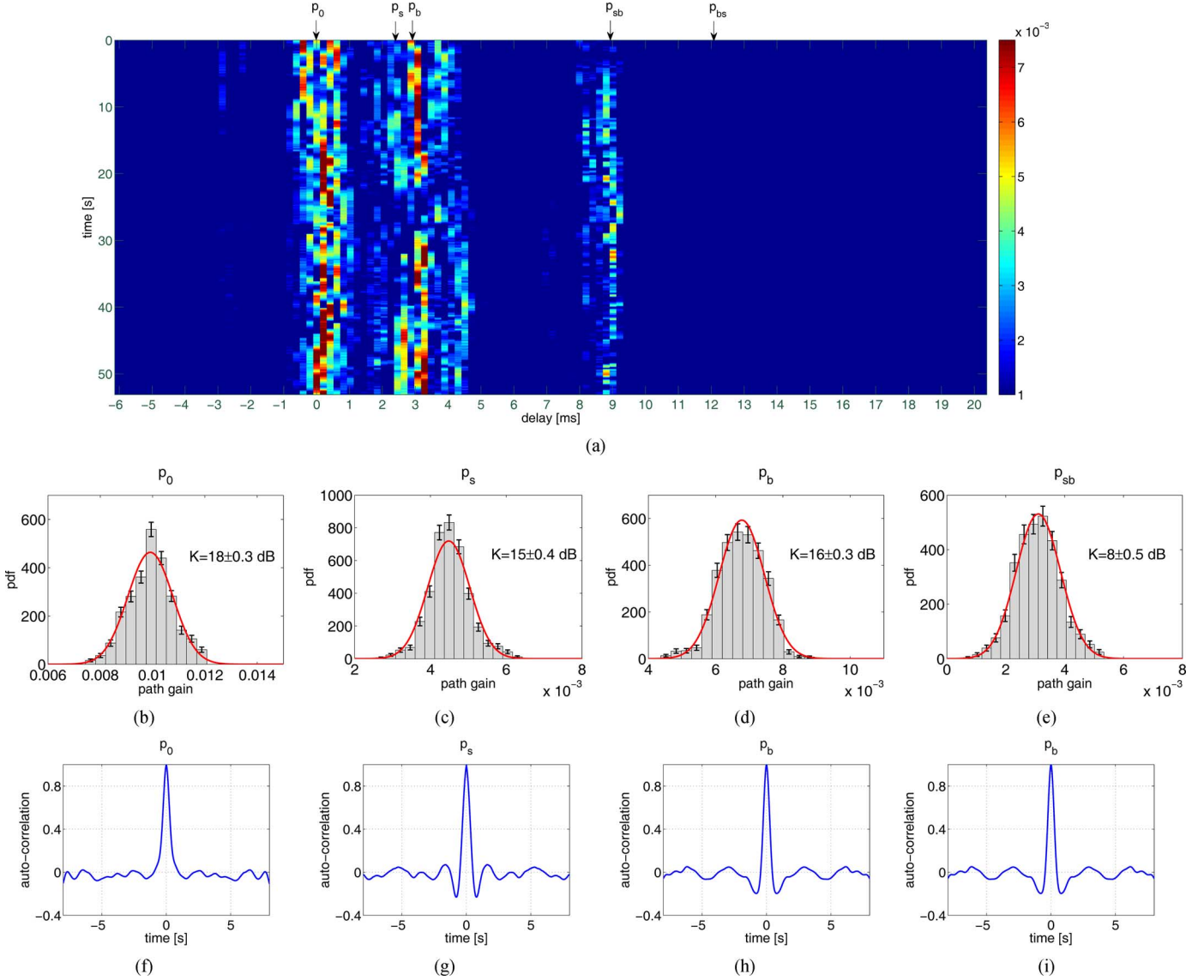
Fig. 8. MACE experiment: (a) time evolution of the magnitude baseband impulse response; (b)–(e) histograms of selected path magnitudes; and (f)–(i) time-correlation functions.

In the PS experiment, the transmission distance was constantly changing as the AUV moved, hence the average gain varied noticeably [Fig. 10(a)]. A continuum of distances was covered during this experiment, as shown in Fig. 10(e). The solid curve there represents the log-distance model (48) whose parameter k_0 is indicated in the figure, while the dots represent the actual gain. Since the AUV was frequently at the same distance from the receiver, there are many values of the actual gain for each distance. The log-distance model parameters were calculated from the data as

$$k_0 = -\frac{\sum_i \hat{\bar{g}}(d_i) 10 \log d_i - \frac{1}{I} \sum_i \hat{\bar{g}}(d_i) \sum_i 10 \log d_i}{\sum_i (10 \log d_i)^2 - \frac{1}{I} \left(\sum_i 10 \log d_i \right)^2}$$

$$g_0 = \frac{1}{I} \sum_i \hat{\bar{g}}(d_i) + k_0 \frac{1}{I} \sum_i 10 \log d_i \qquad (51)$$

where $\hat{\bar{g}}(d_i)$ are the ensemble averages of gains measured at distances d_i, $i = 1, \ldots, I$.

The MACE experiment similarly involved transmission from an AUV. In contrast, signals in the SPACE and KAM experiments were transmitted between fixed points. In the SPACE experiment, the signals were recorded at three different locations (three different transmission distances). Fig. 10(b) shows the time series of the gain for these three locations, while Fig. 10(f) shows the same data clustered around three points along the distance axis. Finally, in the KAM experiment, the signals were recorded at a single location. Hence, a log-distance model is not shown for this experiment.

The following observations are also made about the various experiments.

- Each epoch of the SPACE experiment lasted 3 min, with approximately two idle hours between adjacent epochs. Similarly, 9-min epochs were transmitted every 2 h during the KAM experiment. In Fig. 10(b) and (d), the idle hours are shown as empty spaces between consecutive epochs,
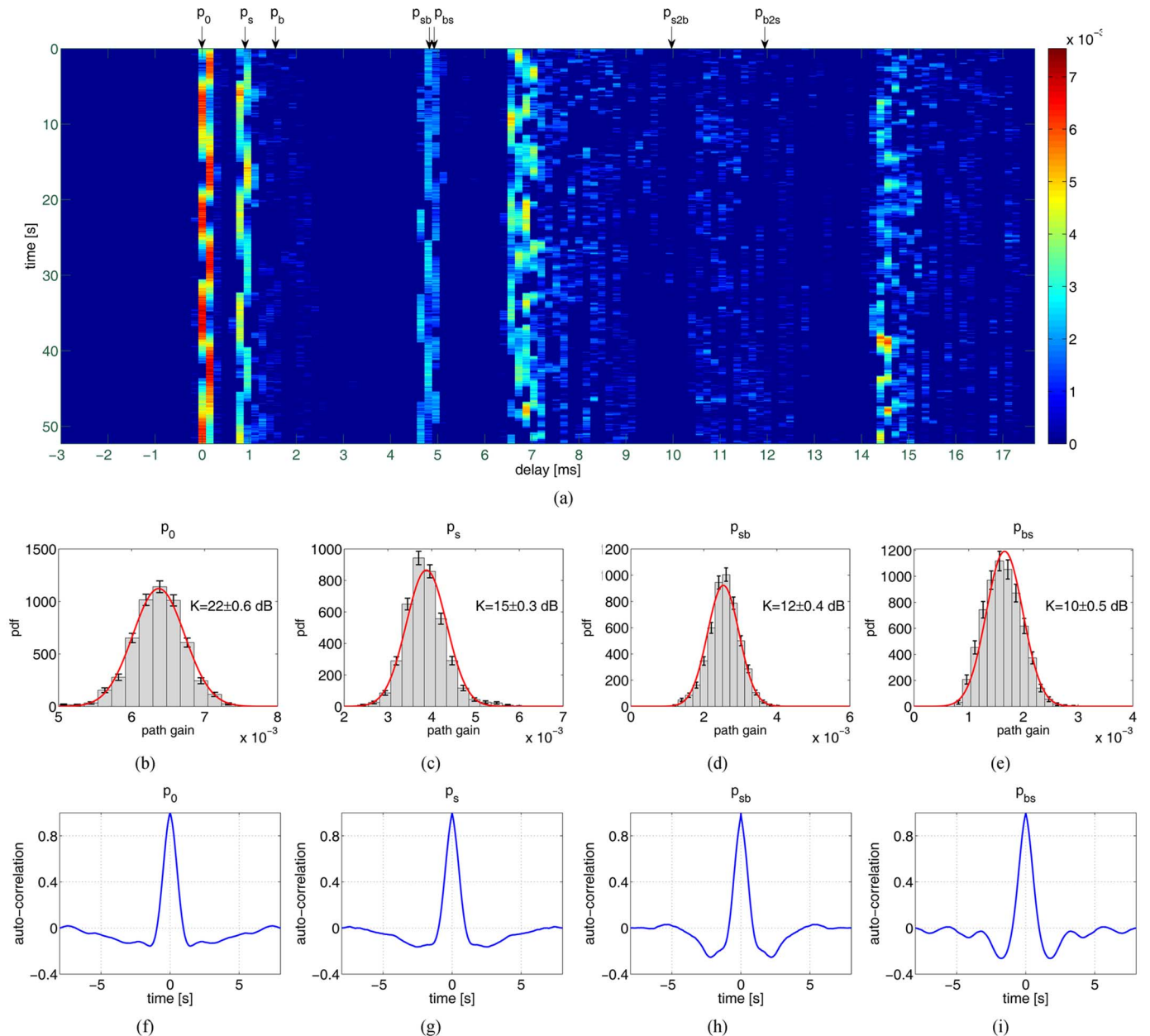
Fig. 9. KAM experiment: (a) time evolution of the magnitude baseband impulse response; (b)–(e) histograms of selected path magnitudes; and (f)–(i) time-correlation functions.

TABLE II
JENSEN–SHANNON DIVERGENCE FOR RICEAN FITS (GRAY ROWS) VERSUS RAYLEIGH FITS (WHITE ROWS)

	direct	reflected 1	reflected 2	reflected 3
SPACE	5.1e-3	3.6e-3	6.6e-3	4.8e-3
	0.185	0.166	0.091	0.064
MACE	5.3e-3	7.4e-3	6.4e-3	3.1e-3
	0.135	0.142	0.151	0.090
KAM	5.1e-4	5.8e-3	5.8e-3	2.9e-3
	0.194	0.162	0.130	0.079

but they are not plotted to scale. The values of the gain for the PS experiment were quantized; hence, they appear at discrete levels in Fig. 10(e).

- The PS and MACE experiments lasted a few hours, while the SPACE and KAM experiments lasted several days, thus undergoing additional time-varying phenomena on a larger

time scale. While the gain variation at each distance does not exceed a few (~5) dB for the PS and MACE experiments, the long-lasting SPACE and KAM experiments experience gain variation of as much as 15 dB over the course of a few days. This observation is notably important, as it indicates that very large savings are available from slow power control.

- In the SPACE experiment, the total (multihour) gain variation is more pronounced at longer distances (15 dB at 1 km, versus 7 dB at 60 m). There also appears to be some correlation between the distances, notably the longer ones (e.g., a decrease in the gain during the final epoch or hour 30). These multihour variations are likely caused by the changing environmental conditions. As the wind/waves/tides change, so do the statistical parameters of the large-scale phenomena.
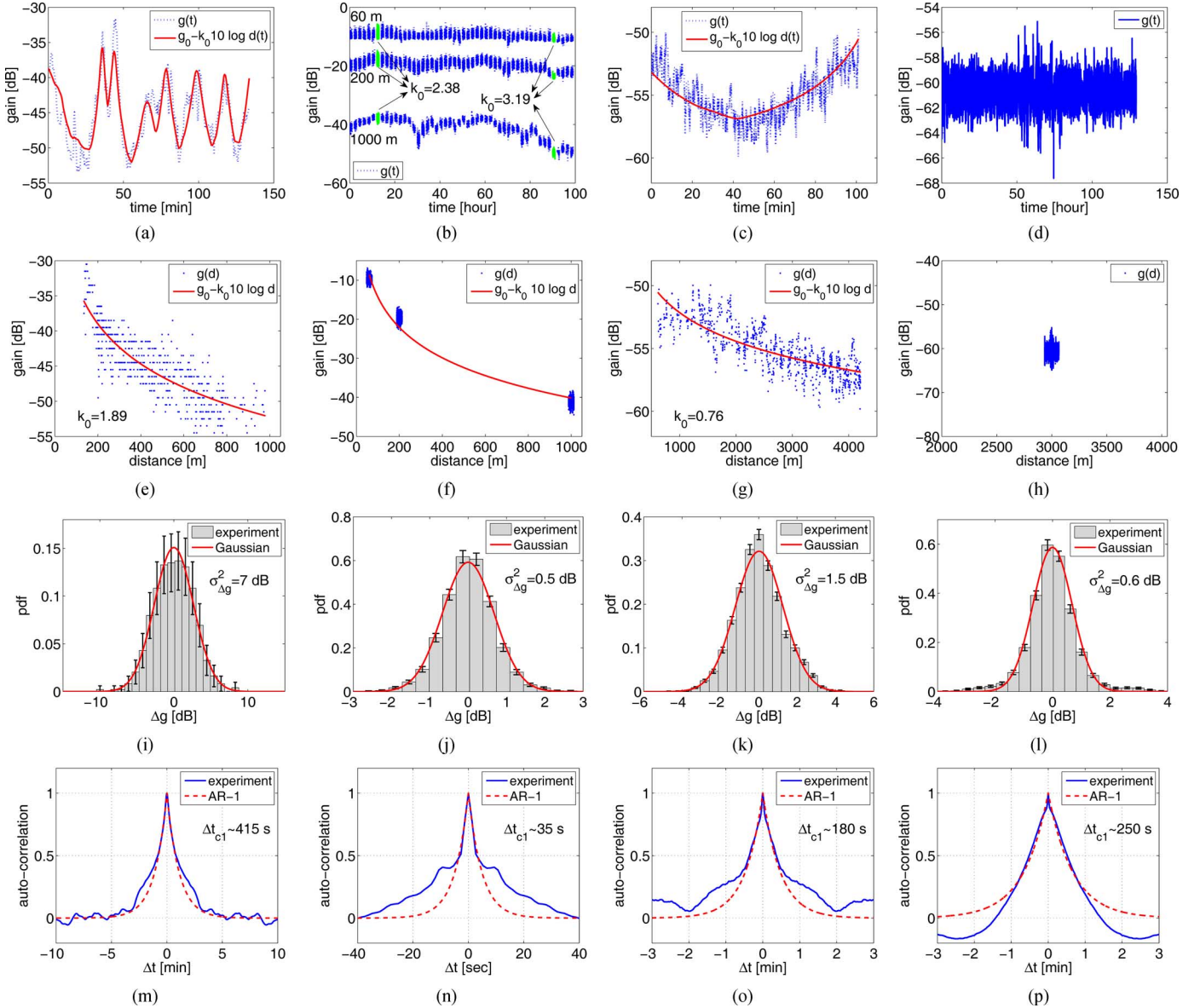
Fig. 10.   Results of large-scale data analysis: PS experiment (left), SPACE (mid-left), MACE (mid-right), and KAM (right). (a)–(d) Gain versus time (dotted) and the model (solid). (e)–(h) Gain versus distance (dotted) and the model (solid). (i)–(l) Histogram of Δg and Gaussian approximation. (m)–(p) Autocorrelation of Δg (solid) and AR-1 autocorrelation (dashed).

- In Fig. 10(b), the values of the large-scale parameter k_0 are indicated for epochs at hours 12 and 90 (highlighted in the figure). In both of the long-lasting experiments, SPACE and KAM, the mean value of the gain is thus calculated separately for each epoch.
- In the MACE experiment, the variance $\sigma_{\Delta g}^2$ estimated during a calm day (evening of June 26, 2010, reported in Fig. 10) was about three times lower than on a windy day (4.8 dB on the morning of June 25, 2010). The corresponding coherence time was twice as long during calm conditions.

Fig. 10(i)–(l) shows the histograms of the random component $\Delta g = g - \bar{g}$, along with a theoretical Gaussian curve with zero mean and variance $\sigma_{\Delta g}^2$ that is estimated from the data and indicated in the figure. Taking into account the pseudostationary nature of the long-lasting experiments (SPACE and KAM), $\bar{g}$ is calculated separately for each epoch. The data suggest that

$\sigma_{\Delta g}^2$ is invariant for the span of distances considered. If greater distance spans are of interest to a particular system, sectioning may be required. Overall, a good match is observed between the histograms and the Gaussian fit, which speaks in favor of the log-normal model for the large-scale channel gain.

Finally, the autocorrelation of Δg is plotted in Fig. 10(m)–(p). Shown also in the plots is an exponentially decaying autocorrelation function $e^{-|\Delta t|/\Delta t_{c1}}$ corresponding to an AR-1 process. A good match is observed between the experimental data and the AR-1 model for small time differences, notably up to several seconds. This fact implies the possibility to predict the channel gain from past samples, the fact that bears an important implication for adaptive power control in acoustic communication systems. Namely, if the round-trip delay is within the coherence time of the channel gain, a feedback loop can be closed between the transmitter and the receiver. Judging by the observations made during the SPACE and KAM experiments, power control

can yield substantial savings (10 dB or more) over longer intervals of time.

VII. Conclusion

In this paper, a statistical model was developed for UWA channels that takes into account physical aspects of acoustic propagation as well as the effects of inevitable random channel variations. Channel variations were classified into small scale and large scale, based on the notion of the underlying random displacement being on the order of a few, or many wavelengths, respectively. While small-scale modeling treats random channel variations over short displacements and, correspondingly, short intervals of time (e.g., subsecond) during which the system geometry and environmental conditions do not change, large-scale modeling treats variations caused by location uncertainty (displacement from the nominal geometry) as well as varying environmental conditions.

The proposed small-scale model describes intrapath dispersion caused by scattering as complex Gaussian multiplicative coefficients with particular correlation properties in time and frequency. Specifically, it was shown that an autoregressive Gaussian displacement of scattering points leads to frequency-dependent exponential time-correlation function of the small-scale fading coefficients, while frequency correlation is dictated by the variance of the intrapath delays. In addition, motion-induced random Doppler shifting, resulting from surface waves or transmitter/receiver drifting, was shown to lead to Bessel-type autocorrelation functions. Based on such a model, a computationally efficient channel simulator was proposed, in which each path's small-scale coefficient is represented as an autoregressive Gaussian process itself, and provision is made to account for frequency correlation across the signal bandwidth.

Large-scale modeling focused on the channel gain, which offers a measure of the received signal strength averaged locally over small-scale phenomena. A log-normal model was proposed for the large-scale gain, whose mean follows a log-distance dependence. Experimental data from four deployment sites with varying degrees of mobility were used for a statistical analysis. Probability distributions and correlation functions of the salient small- and large-scale parameters demonstrated a good match with the theoretical models.

The present model is based on the Gaussian assumption for the underlying processes, which is a starting point from a statistical point of view, although likely not the last word on this topic. Future work will also focus on examining frequency-correlation properties of the small-scale fading in wideband experimental systems, as well as on extending the proposed models to address spatial correlation properties of the acoustic channel on both small and large scales.

References

[1] M. B. Porter, "Bellhop code," [Online]. Available: http://oalib.hlsresearch.com/Rays/index.html

[2] J. C. Peterson and M. B. Porter, "Ray/beam tracing for modeling the effects of ocean and platform dynamics," *IEEE J. Ocean. Eng.*, vol. 38, no. 4, Oct. 2013, DOI: 10.1109/JOE.2013.2278914.

[3] C. T. Tindle, "Wavefronts and waveforms in deep-water sound propagation," *J. Acoust. Soc. Amer.*, vol. 112, no. 2, pp. 464–475, 2002.

[4] G. B. Deane, J. C. Preisig, C. T. Tindle, A. Lavery, and M. D. Stokes, "Deterministic forward scatter from surface gravity waves," *J. Acoust. Soc. Amer.*, vol. 132, no. 6, pp. 3673–3686, 2012.

[5] P. Qarabaqi and M. Stojanovic, "Statistical modeling of a shallow water acoustic communication channel," in *Proc. Underwater Acoust. Meas. Conf.*, Nafplion, Greece, Jun. 2009, pp. 1341–1350.

[6] F. Socheleau, J. Passerieux, and C. Laot, "Characterisation of time-varying underwater acoustic communication channel with application to channel capacity," presented at the Underwater Acoust. Meas. Conf., Nafplion, Greece, Jun. 2009.

[7] A. Radosevic, J. Proakis, and M. Stojanovic, "Statistical characterization and capacity of shallow water acoustic channels," in *Proc. IEEE OCEANS Eur. Conf.*, 2009, DOI: 10.1109/OCEANSE.2009.5278349.

[8] R. Galvin and R. E. W. Coats, "A stochastic underwater acoustic channel model," in *Proc. MTS/IEEE OCEANS Conf.*, Sep. 1996, vol. 1, pp. 203–210.

[9] P. Qarabaqi and M. Stojanovic, "Modeling the large scale transmission loss in underwater acoustic channels," in *Proc. 49th Annu. Allerton Conf. Commun. Control Comput.*, Sep. 2011, pp. 445–452.

[10] B. Tomasi, P. Casari, L. Badia, and M. Zorzi, "A study of incremental redundancy hybrid ARQ over Markov channel models derived from experimental data," in *Proc. 5th ACM Int. Workshop UnderWater Netw.*, Woods Hole, MA, USA, Sep. 2010, DOI: 10.1145/1868812.1868816.

[11] W. B. Yang and T. C. Yang, "High-frequency channel characterization for M-ary frequency-shift-keying underwater acoustic communications," *J. Acoust. Soc. Amer.*, vol. 120, no. 5, pp. 2615–2626, Nov. 2006.

[12] J. Zhang, J. Cross, and Y. R. Zheng, "Statistical channel modeling of wireless shallow water acoustic communications from experiment data," in *Proc. Military Commun. Conf.*, 2010, pp. 2412–2416.

[13] M. Chitre, "A high-frequency warm shallow water acoustic communications channel model and measurements," *J. Acoust. Soc. Amer.*, vol. 122, no. 5, pp. 2580–2586, Nov. 2007.

[14] B. Tomasi, G. Zappa, K. McCoy, P. Casari, and M. Zorzi, "Experimental study of the space-time properties of acoustic channels for underwater communications," in *Proc. IEEE OCEANS Conf.*, 2010, DOI: 10.1109/OCEANSSYD.2010.5603667.

[15] F. Socheleau, C. Laot, and J. Passerieux, "Stochastic replay of non-WSSUS underwater acoustic communication channels recorded at sea," *IEEE Trans. Signal Process.*, vol. 59, no. 10, pp. 4838–4849, Oct. 2011.

[16] F. Ruiz-Vega, M. C. Clemente, P. Otero, and J. F. Paris, "Rician shadowed statistical characterization of shallow water acoustic channels," presented at the Underwater Commun., Channel Model. Validation, Sestri-Levante, Italy, Sep. 2012.

[17] R. M. Heitsenrether and M. Badiey, "Modeling acoustic signal fluctuations induced by sea surface roughness," *Proc. AIP Conf.*, vol. 728, pp. 214–221, 2004.

[18] J. C. Preisig and G. B. Deane, "Surface wave focusing and acoustic communications in the surf zone," *J. Acoust. Soc. Amer.*, vol. 116, no. 4, pp. 2067–2080, 2004.

[19] G. Deane, "The suspension of large bubbles near the sea surface by turbulence and their role in absorbing forward-scattered sound," *IEEE J. Ocean. Eng.*, vol. 38, no. 4, Oct. 2013, DOI: 10.1109/JOE.2013.2257573.

[20] L. M. Brekhovskikh and Y. P. Lysanov, *Fundamentals of Ocean Acoustics*, 3rd ed. New York, NY, USA: Springer-Verlag, 2003.

[21] A. Radosevic, R. Ahmed, T. Duman, J. Proakis, and M. Stojanovic, "Adaptive OFDM modulation for underwater acoustic communications: Design considerations and experimental results," *IEEE J. Ocean. Eng.*, 2013, DOI: 10.1109/JOE.2013.2253212.

[22] P. Cardieri and T. S. Rappaport, "Statistics of the sum of lognormal variables in wireless communications," in *Proc. IEEE Veh. Technol. Conf.*, Tokyo, Japan, May 15–18, 2000, pp. 1823–1827.

[23] Woods Hole Oceanographic Institution (WHOI), "Micro-modem overview," Woods Hole, MA, USA [Online]. Available: http://acomms.whoi.edu/umodem/

[24] W. Li and J. C. Preisig, "Estimation of rapidly time-varying sparse channels," *IEEE J. Ocean. Eng.*, vol. 32, no. 4, pp. 927–939, Oct. 2007.

[25] P. Phillips and P. Perron, "Testing for a unit root in time series regression," *Biometrika*, vol. 75, pp. 335–346, 1988.

[26] J. Lin, "Divergence measures based on the Shannon entropy," *IEEE Trans. Inf. Theory*, vol. 37, no. 1, pp. 145–151, Jan. 1991.

Parastoo Qarabaqi (S'07) received the B.S. degree in electrical engineering from Sharif University of Technology, Tehran, Iran, in 2007. She is currently working toward the Ph.D. degree in electrical and computer engineering at Northeastern University, Boston, MA, USA.

Her research interests include wireless communications, statistical and adaptive signal processing, and their applications to underwater acoustic communications.

Milica Stojanovic (SM'08–F'10) graduated from the University of Belgrade, Belgrade, Serbia, in 1988 and received the M.S. and Ph.D. degrees in electrical engineering from Northeastern University, Boston, MA, USA, in 1991 and 1993, respectively.

She was a Principal Scientist at the Massachusetts Institute of Technology (MIT), Cambridge, MA, USA, until 2008, when she joined Northeastern University, where she is currently a Professor of Electrical and Computer Engineering. She is also a Guest Investigator at the Woods Hole Oceanographic Institution (WHOI), Woods Hole, MA, USA, and a Visiting Scientist at MIT. Her research interests include digital communications theory, statistical signal processing and wireless networks, and their applications to underwater acoustic systems.

Prof. Stojanovic is an Associate Editor for the IEEE JOURNAL OF OCEANIC ENGINEERING and the IEEE TRANSACTIONS ON SIGNAL PROCESSING. She is an Advisory Board Member of the IEEE COMMUNICATION LETTERS, an Editorial Board Member of the *Elsevier Physical Communication Journal*, and Chair of the IEEE Ocean Engineering Society's Technical Committee for Underwater Communications.